

# Atomic Layer Etching Mechanism of MoS<sub>2</sub> for Nanodevices

Ki Seok Kim,<sup>†</sup> Ki Hyun Kim,<sup>†</sup> Yeonsig Nam,<sup>‡</sup> Jaeho Jeon,<sup>§</sup> Soonmin Yim,<sup>||</sup> Eric Singh,<sup>†,⊥</sup> Jin Yong Lee,<sup>‡,†</sup> Sung Joo Lee,<sup>§</sup><sup>ID</sup> Yeon Sik Jung,<sup>||</sup><sup>ID</sup> Geun Young Yeom,<sup>\*,†,§</sup><sup>ID</sup> and Dong Woo Kim<sup>\*,†</sup>

<sup>†</sup>School of Advanced Materials Science and Engineering, <sup>‡</sup>School of Chemistry, and <sup>§</sup>SKKU Advanced Institute of Nano Technology (SAINT), Sungkyunkwan University, 2066 Seobu-ro, Jangan-gu, Suwon-si, Gyeonggi-do 16419, Republic of Korea

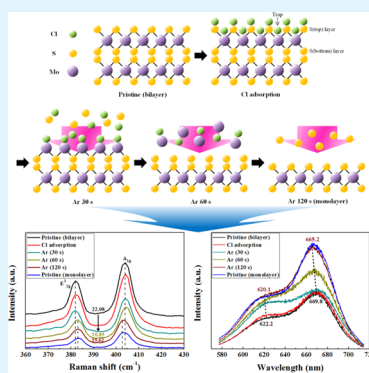
<sup>||</sup>School of Materials Science and Engineering, Korea Advanced Institute of Science and Technology (KAIST), 291 Daehak-ro, Yuseong-gu, Daejeon 305-701, Republic of Korea

<sup>⊥</sup>Department of Computer Science, Stanford University, Stanford, California 94305, United States

## Supporting Information

**ABSTRACT:** Among the layered transition metal dichalcogenides (TMDs) that can form stable two-dimensional crystal structures, molybdenum disulfide (MoS<sub>2</sub>) has been intensively investigated because of its unique properties in various electronic and optoelectronic applications with different band gap energies from 1.29 to 1.9 eV as the number of layers decreases. To control the MoS<sub>2</sub> layers, atomic layer etching (ALE) (which is a cyclic etching consisting of a radical-adsorption step such as Cl adsorption and a reacted-compound-desorption step via a low-energy Ar<sup>+</sup>-ion exposure) can be a highly effective technique to avoid inducing damage and contamination that occur during the reactive steps. Whereas graphene is composed of one-atom-thick layers, MoS<sub>2</sub> is composed of three-atom-thick S<sub>(top)</sub>—Mo<sub>(mid)</sub>—S<sub>(bottom)</sub> layers; therefore, the ALE mechanisms of the two structures are significantly different. In this study, for MoS<sub>2</sub> ALE, the Cl radical is used as the adsorption species and a low-energy Ar<sup>+</sup> ion is used as the desorption species. A MoS<sub>2</sub> ALE mechanism (by which the S<sub>(top)</sub>, Mo<sub>(mid)</sub>, and S<sub>(bottom)</sub> atoms are sequentially removed from the MoS<sub>2</sub> crystal structure due to the trapped Cl atoms between the S<sub>(top)</sub> layer and the Mo<sub>(mid)</sub> layer) is reported according to the results of an experiment and a simulation. In addition, the ALE technique shows that a monolayer MoS<sub>2</sub> field effect transistor (FET) fabricated after one cycle of ALE is undamaged and exhibits electrical characteristics similar to those of a pristine monolayer MoS<sub>2</sub> FET. This technique is also applicable to all layered TMD materials, such as tungsten disulfide (WS<sub>2</sub>), molybdenum diselenide (MoSe<sub>2</sub>), and tungsten diselenide (WSe<sub>2</sub>).

**KEYWORDS:** transition metal dichalcogenides (TMDs), molybdenum disulfide (MoS<sub>2</sub>), atomic layer etching (ALE), low-energy Ar<sup>+</sup>-ion, field effect transistors (FETs)



## INTRODUCTION

Layered transition metal dichalcogenides (TMDs) have attracted considerable attention in various electronic and optoelectronic applications due to their unique properties.<sup>1–3</sup> Among the layered TMD materials such as molybdenum disulfide (MoS<sub>2</sub>), tungsten disulfide (WS<sub>2</sub>), molybdenum diselenide (MoSe<sub>2</sub>), and tungsten diselenide (WSe<sub>2</sub>), which can form a stable crystal structure,<sup>4</sup> MoS<sub>2</sub> has been intensively investigated due to its distinctive electronic, optical, and catalytic properties, as well as for its use in dry lubrication. MoS<sub>2</sub> possesses covalent bonds between the Mo and S atoms, whereas the MoS<sub>2</sub> layers are combined through van der Waals forces.<sup>5–8</sup> In addition, the electronic properties are extremely dependent on the number of layers, whereby different band-gap energies are exhibited from 1.29 to 1.9 eV as the number of layers is decreased.<sup>9–11</sup>

Accordingly, the technology involved in controlling the MoS<sub>2</sub> layers is extremely important in various nanodevice applications. However, difficulty is encountered with controlling the layers of MoS<sub>2</sub> when conventional synthetic methods are used,

such as the chemical vapor deposition (CVD),<sup>12–14</sup> plasma-enhanced CVD (PECVD),<sup>15</sup> and exfoliation methods. This difficulty arises because these methods generally involve random nucleation of nonuniform MoS<sub>2</sub> domains with different number of layers.<sup>16,17</sup> Therefore, not only multilayer MoS<sub>2</sub> but also MoS<sub>2</sub> that has areas with different layer thicknesses is generally formed on the same wafer, especially when the wafer size is of a commercial scale. For this reason, various methods have been reported by many research groups for the control of the MoS<sub>2</sub> layers, such as xenon difluoride (XeF<sub>2</sub>) etching,<sup>8</sup> laser thinning,<sup>16</sup> Ar-plasma etching,<sup>18</sup> thermal annealing,<sup>19,20</sup> and soft plasma etching that uses low-energy electrons (<0.4 eV) for SF<sub>6</sub>/N<sub>2</sub> plasmas to minimize the ion-bombardment-related damage.<sup>17</sup> However, these methods are ineffective for the precise layer-by-layer control of MoS<sub>2</sub> layers at the atomic scale because the control of the MoS<sub>2</sub> layers depends only on the

Received: December 11, 2016

Accepted: March 17, 2017

Published: March 17, 2017

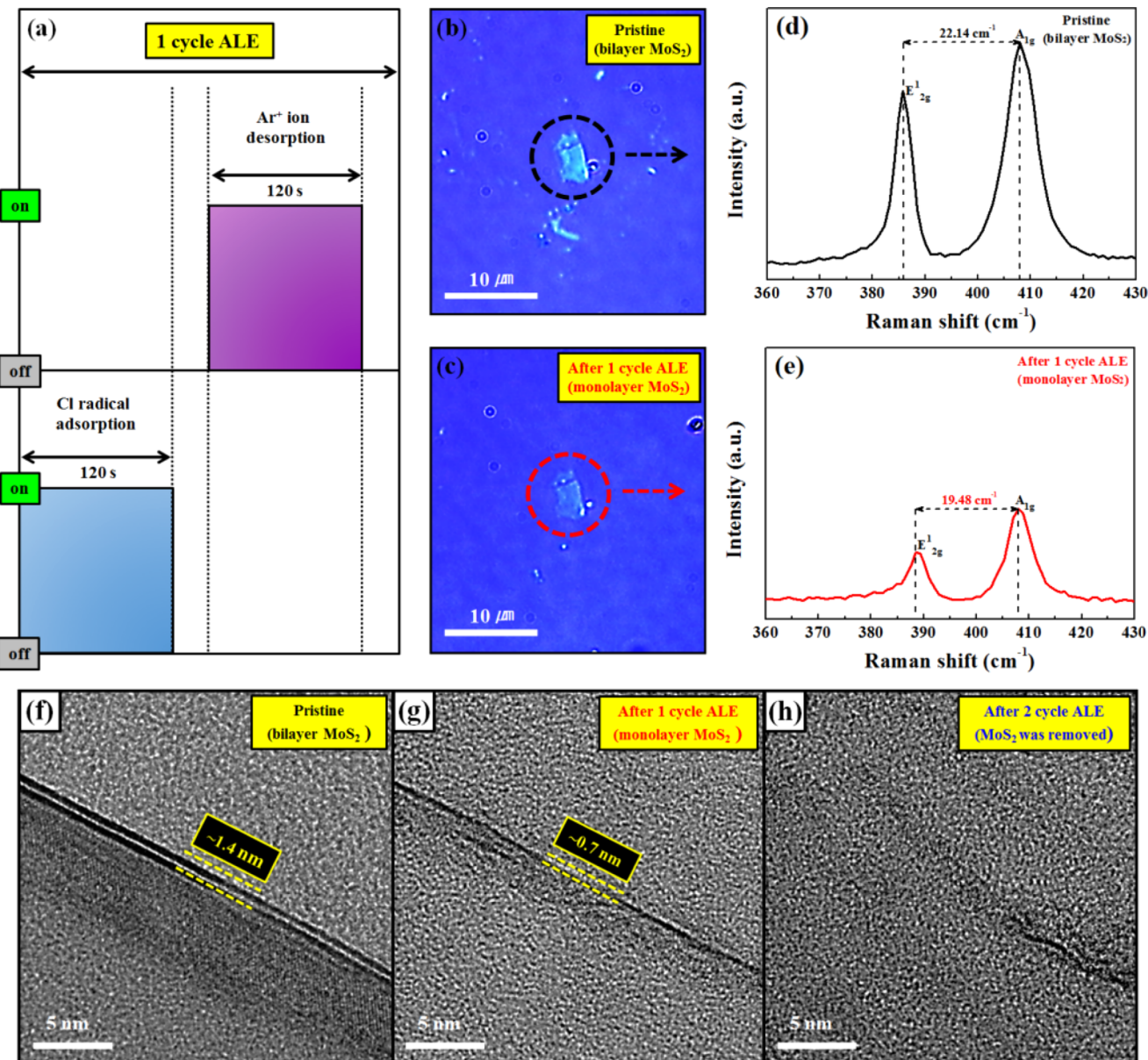


**Figure 1.** (a) Schematic diagram of the MoS<sub>2</sub> one-cycle ALE composed of the Cl-radical adsorption step and the subsequent Ar<sup>+</sup>-ion desorption step. (b), (c) Optical microscopic images of the pristine exfoliated bilayer MoS<sub>2</sub> and monolayer MoS<sub>2</sub> after one ALE cycle, as shown in (a). (d, e) Raman spectroscopic data of the pristine bilayer MoS<sub>2</sub> and monolayer MoS<sub>2</sub> that were observed after the one-cycle ALE. (f–h) TEM cross-sectional images of the pristine bilayer MoS<sub>2</sub>: (f) as received, (g) after one-cycle ALE, and (h) after two-cycle ALE, exhibiting the removal of one monolayer per cycle.

thinning time and because processing without inducing damage is difficult.

On the contrary, atomic layer etching (ALE) is one of the most important techniques that allows for a precise control of the number of MoS<sub>2</sub> layers without inducing damage and contamination through the chemical adsorption and physical desorption of the cyclic steps. In our previous work, we reported the successful layer-by-layer etching of MoS<sub>2</sub> through controlled Cl-radical adsorption using an inductively coupled plasma (ICP) system with a mesh grid and Ar<sup>+</sup>-ion desorption using a two-grid Ar<sup>+</sup>-ion source system with a monoenergetic energy of 20 eV. However, the ALE mechanism of a single-monolayer MoS<sub>2</sub> consisting of a S—Mo—S crystal structure could not be identified.<sup>21</sup>

Whereas a single monolayer of graphene is composed of a one-atom-thick layer, a single monolayer of TMDs is composed

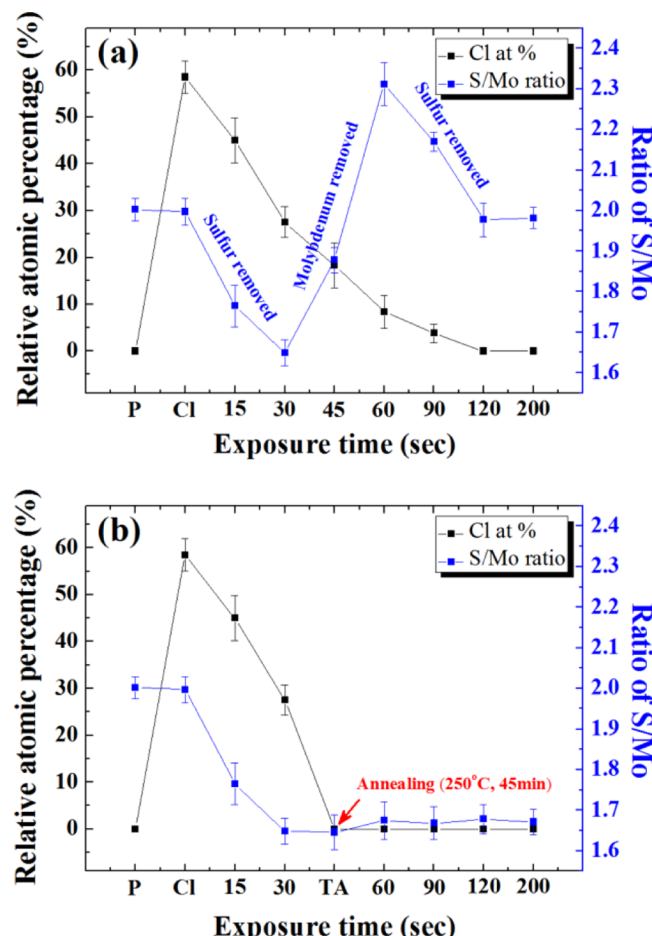
of a three-atom-thick layer; therefore, the ALE mechanisms of the two structures significantly differ. In this research, we present the ALE mechanism of a single-monolayer MoS<sub>2</sub> from a bilayer MoS<sub>2</sub> through sequential Cl-radical adsorption and Ar<sup>+</sup>-ion desorption. This novel ALE technique allows uniform removal of a single-monolayer MoS<sub>2</sub> without undesirable residues and damage to the etched surface. In addition, the ALE technique can be performed at a low temperature, has a high throughput, covers a large area, and is a Si-compatible process, in contrast to the other previous MoS<sub>2</sub> etch methods. In addition, using the ALE method, it is possible to control the S/Mo ratio of the top MoS<sub>2</sub> layer during the Ar<sup>+</sup>-ion desorption step and is very useful for making nanodevices of next-generation layered TMD materials.

## RESULTS AND DISCUSSION

Figure 1a shows a schematic diagram of the cyclic etching process that is composed of a sequential reactant-adsorption step and a reacted-compound-desorption step for the one-cycle MoS<sub>2</sub> ALE. Figure 1b,c shows the optical microscopic images of the pristine bilayer MoS<sub>2</sub> and the monolayer MoS<sub>2</sub>, respectively, after the one-cycle ALE of the bilayer MoS<sub>2</sub>. Figure 1d,e shows the Raman spectroscopic data of the pristine bilayer MoS<sub>2</sub> and the monolayer MoS<sub>2</sub>, respectively, that were obtained after the one-cycle ALE shown in Figure 1a. Through the adsorption of the reactive Cl radical on the bilayer MoS<sub>2</sub> surface for 120 s during the adsorption step and through the subsequent Ar<sup>+</sup>-ion exposure with an adequate energy of ~20 eV (Figure S1a of the Supporting Information) for 120 s during the desorption step, a monolayer MoS<sub>2</sub> could be obtained (i.e., the monolayer MoS<sub>2</sub> could be removed) from the bilayer MoS<sub>2</sub> by the one-cycle ALE;<sup>21</sup> however, when the bilayer MoS<sub>2</sub> was processed with the Cl-radical-adsorption step for only 10 min or with the Ar<sup>+</sup>-ion desorption step for only 10 min, a change of the Raman spectroscopic data was not observed, indicating that the etching of the bilayer MoS<sub>2</sub> did not occur with only Cl-radical adsorption or with only Ar<sup>+</sup>-ion bombardment (Figure S1b). Therefore, using ALE, the thickness of the MoS<sub>2</sub> layers could be precisely controlled (Figure S1c–f). Also, the MoS<sub>2</sub> thickness was observed for the as-received bilayer MoS<sub>2</sub> after the one-cycle ALE and after the two-cycle ALE using cross-sectional TEM. As shown in Figure 1f–h, the removal of exactly one MoS<sub>2</sub> monolayer per ALE cycle could be confirmed. In this study, the ALE mechanism of the MoS<sub>2</sub> layers was further investigated.

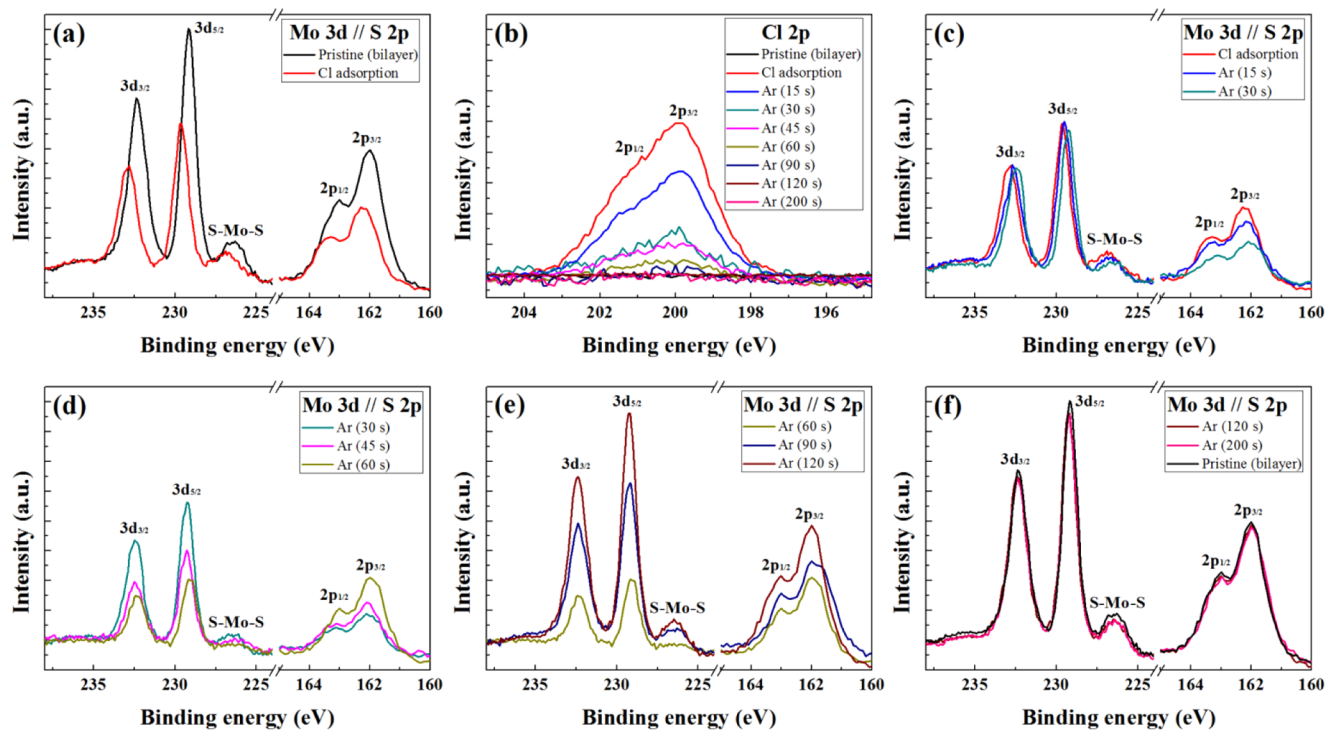
During MoS<sub>2</sub> ALE, when the MoS<sub>2</sub>-layer surface is exposed to the Cl radicals, the Cl radicals fully cover the MoS<sub>2</sub> surface and are chemisorbed onto the MoS<sub>2</sub> surface. Also, when the Ar<sup>+</sup> ions of an adequate energy bombard the surface, the chemically adsorbed MoS<sub>2</sub>-surface layer is gradually removed by desorption until the top monolayer MoS<sub>2</sub> is removed, exposing the MoS<sub>2</sub> layer underneath. The single MoS<sub>2</sub> monolayer is composed of three atomic layers (i.e., S—Mo—S); therefore, it is important to determine how this three-atom-thick monolayer is removed during the desorption step. The change of the MoS<sub>2</sub>-layer surface composition with the desorption time and the Ar<sup>+</sup>-ion exposure time was investigated using a bilayer MoS<sub>2</sub> that was prepared by CVD. In particular, the way in which the top S, middle Mo, and bottom S atoms of the chlorinated MoS<sub>2</sub> are removed during the desorption step was closely investigated.

Figure 2a shows the change of the S/Mo ratio and the relative Cl atomic percentage on the MoS<sub>2</sub> surface that was measured as a function of the Ar<sup>+</sup>-ion exposure time (15–200 s) using X-ray photoelectron spectroscopy (XPS) during the desorption step of MoS<sub>2</sub> ALE after Cl-radical adsorption on the MoS<sub>2</sub> surface for the bilayer MoS<sub>2</sub>. As shown, before the exposure to the Ar<sup>+</sup> ion after the Cl-radical adsorption step for MoS<sub>2</sub> ALE, the ratio of S/Mo is ~2.0, indicating that the stoichiometric MoS<sub>2</sub> had not changed even with Cl-radical adsorption of the relative atomic percentage of 58.5%. The binding energies of the four top and four bottom S atoms (S<sub>1–4</sub>) that were bound with a single Mo atom of the first MoS<sub>2</sub> layer were investigated (Figure S3) after Cl-radical adsorption on one of the top S atoms (top S; S<sub>1 or 3</sub>). The binding energy of the top S<sub>(1 or 3)</sub> atoms was decreased significantly from 1.993 to 1.472 eV by the movement of electrons from S to Cl due to



**Figure 2.** (a) Change of the S/Mo ratio and the relative Cl atomic percentage on the MoS<sub>2</sub> surface that was measured as a function of the Ar<sup>+</sup>-ion exposure time (15–200 s) using XPS during the desorption step of MoS<sub>2</sub> ALE for the bilayer MoS<sub>2</sub>. (b) Change of the S/Mo ratio and the relative Cl atomic percentage on the MoS<sub>2</sub> surface that was measured as a function of the Ar<sup>+</sup>-ion exposure time up to 30 s, similar to (a). A further exposure to the Ar<sup>+</sup> ion of 200 s was performed after the annealing (TA); after 30 s of Ar<sup>+</sup>-ion exposure time (at 30 s, it appeared that the top S of the MoS<sub>2</sub> had been removed), a further Ar<sup>+</sup>-ion desorption was carried out after the MoS<sub>2</sub> sample was annealed at 250 °C for 45 min in a vacuum to remove the Cl radical on the MoS<sub>2</sub> surface. The experiment was repeated seven times, and the data were averaged. P indicates the pristine MoS<sub>2</sub> state, and Cl represents MoS<sub>2</sub> after Cl-radical adsorption.

the higher electronegativity of Cl compared to that of S, whereas a change of the binding energies of the bottom S atoms (bottom S; S<sub>2 or 4</sub>) was not observed (Figure S4 and Table S1). Therefore, this shows that, for the Cl-adsorbed MoS<sub>2</sub>, the top S atoms will be removed first by the exposure to the Ar<sup>+</sup> ions. In addition, during the Cl-radical adsorption step, the Cl atoms can also be trapped between the top S atoms and the mid Mo atoms by the van der Waals force. These Cl atoms can form a Mo—Cl bond during the desorption step caused by the Ar<sup>+</sup>-ion exposure (Figure S5). As shown in Figure 2a, with the increase of the Ar<sup>+</sup>-ion exposure time from 0 to 30 s, the S/Mo ratio was decreased gradually from 2 to ~1.65, in addition to the decrease of the relative Cl percentage from 58.5 to ~27.5% due to the preferential removal of the top S atoms that had bonded to the Cl with the lowest binding energy in the top MoS<sub>2</sub> layer.



**Figure 3.** XPS data of Mo, S, and Cl on the  $\text{MoS}_2$  surface after Cl-radical adsorption and during  $\text{Ar}^+$ -ion desorption of  $\text{MoS}_2$  ALE. (a) XPS data of the pristine bilayer  $\text{MoS}_2$  before and after Cl-radical adsorption. (b) XPS data of Cl before/after Cl-radical adsorption and after the  $\text{Ar}^+$ -ion exposure time of 0–200 s. XPS data of Mo and S after the  $\text{Ar}^+$ -ion exposure of the Cl-adsorbed bilayer  $\text{MoS}_2$  for (c) 0, 15, 30 s, (d) 30, 45, 60 s, (e) 60, 90, 120 s, and (f) 120, 200 s, and pristine bilayer  $\text{MoS}_2$ .

When the  $\text{Ar}^+$ -ion exposure time was increased from 30 to 60 s, the S/Mo ratio was increased from  $\sim 1.65$  to  $\sim 2.31$ , indicating the removal of Mo below the top S atoms. The relative Cl percentage continuously decreased from 27.5% at 30 s to approximately 8.4% at 90 s, indicating the removal of Mo by Mo—Cl. The simulation results (Figure S6 and Table S2) show that when the Mo atoms are bonded with the trapped/adsorbed Cl atoms after the top S atoms were removed the Mo-binding energy decreased from 2.147 to 1.630 eV, whereas the binding energy of the Mo atoms further increased from 2.147 to 2.616 eV due to the tighter binding with the bottom S atoms when the Mo atoms are not bonded to the trapped Cl atoms. The binding energy of the bottom S atoms did not change significantly after the top S atoms were removed, and it remained higher than that of the Mo atoms that were bonded with Cl. Therefore, the increased S/Mo ratio for the  $\text{Ar}^+$ -ion exposure time of 30–60 s should be related to the removal of Mo—Cl that formed on the first  $\text{MoS}_2$  layer during Cl-radical adsorption.

However, when the  $\text{Ar}^+$ -ion exposure time was further increased from 60 to 120 s, the S/Mo ratio was again decreased from  $\sim 2.31$  to  $\sim 2$ , indicating the removal of the bottom S atoms after the removal of the Mo atoms in the first  $\text{MoS}_2$  layer. After the removal of the Mo in the first  $\text{MoS}_2$  layer, only the bottom S atoms remained. After the removal of the Mo atoms, the binding energy of the bottom S atoms (bottom  $S_{(2 \text{ or } 4)}$  atoms can be bonded together, provided the van der Waals force is maintained between the bottom S atoms and the second  $\text{MoS}_2$  layer) decreases further from  $\sim 1.91$  to  $\sim 1.51$  eV (Figure S7 and Table S3) and the bottom S atoms are preferentially removed by the  $\text{Ar}^+$  exposure from 60 to 120 s. The relative Cl percentage decreased from 8.4 to 0% during the  $\text{Ar}^+$ -ion exposure from 60 to 120 s. It is believed that the

remaining 8.4% of the Cl atoms at 90 s are related to the bonding of some of the Cl atoms (possibly by the dissociation of the removed Mo—Cl) to the bottom S atoms. The remaining Cl percentage also decreased to 0 after the  $\text{Ar}^+$ -ion exposure of 120 s, indicating the exposure of the fresh second  $\text{MoS}_2$  layer.

After the preferential removal of the bottom  $S_{(2 \text{ or } 4)}$  atoms, the second  $\text{MoS}_2$  layer was exposed. However, even though the  $\text{Ar}^+$ -ion exposure time was extended to 200 s after the first  $\text{MoS}_2$  layer was completely removed at 120 s, the S/Mo ratio remained at  $\sim 2$ , indicating that the second  $\text{MoS}_2$  layer was not etched by the  $\text{Ar}^+$ -ion energy of 20 eV (Figure S1b). The simulation results are based on the A–A stacking of the bilayer  $\text{MoS}_2$ , but the same results were obtained for the A–B stacking of the bilayer  $\text{MoS}_2$  (Figure S8 and Table S4).

To investigate the importance of Cl-radical adsorption between the top S atoms and the Mo atoms in  $\text{MoS}_2$  during the desorption step of  $\text{MoS}_2$  ALE, the remaining 27.5% of Cl atoms on the first  $\text{MoS}_2$  layer after 30 s of the  $\text{Ar}^+$ -ion exposure, that is, after the removal of the top S atoms in the first  $\text{MoS}_2$  layer, were removed by annealing in a vacuum ( $250^\circ\text{C}$ , 45 min) and the annealed  $\text{MoS}_2$  sample was further exposed to the  $\text{Ar}^+$  ions at 200 s. The S/Mo ratio and the relative Cl percentage that was measured by XPS are shown in Figure 2b. As shown in Figure 2b, after the annealing, the atomic percentage of the Cl atoms of the  $\text{MoS}_2$  layer decreased to 0% due to the vaporization of the trapped/adsorbed Cl atoms from the first- $\text{MoS}_2$ -layer surface (the  $\text{MoS}_2$  layer after the top S atoms were removed). On the other hand, the S/Mo ratio remained the same as that before the annealing, indicating the removal of only the Cl atoms on the surface by annealing. It is believed that the preferential removal of Cl on the first- $\text{MoS}_2$ -layer surface is related to the lower binding energy of Cl (0.881

eV) when compared to that of Mo (1.630 eV) in the  $\text{MoS}_2$  structure (Figure S6 and Table S2). After the removal of Cl on the first- $\text{MoS}_2$ -layer surface, the  $\text{Mo}^{6+}$  peak at  $\sim 236$  eV was observed on the  $\text{MoS}_2$  surface in the XPS analysis, in addition to the redshifts of the Mo peaks ( $3\text{d}_{3/2}$  and  $3\text{d}_{5/2}$ ) and the S peaks ( $2\text{p}_{1/2}$  and  $2\text{p}_{3/2}$ ) (Figure S9). The  $\text{Mo}^{6+}$  peak is related to a defective  $\text{MoS}_2$  (i.e.,  $\text{MoS}_x$ ,  $1 \leq x \leq 2$ ), and it is formed by the binding of only the Mo atoms with the bottom S atoms after the removal of the Cl atoms on the first  $\text{MoS}_2$  layer (the first  $\text{MoS}_2$  layer after the top S atoms are removed). The removal of Cl from the  $\text{MoS}_2$  surface also causes redshifts of the XPS peaks that are related to Mo and S. As mentioned earlier, after the top S atoms are removed, the binding energy between the Mo and the bottom S atoms increased to 2.616 eV when no Cl atoms are adsorbed on Mo. Therefore, as shown in Figure 2b, for the annealed  $\text{MoS}_2$ , the S/Mo ratio was not changed even after the  $\text{Ar}^+$ -ion exposure for 200 s due to the high binding energy between the Mo and bottom S atoms. This indicates that no further etching of  $\text{MoS}_2$  occurred and reveals the importance of Cl-radical adsorption on the Mo surface during Mo ALE. In fact, the increase of the  $\text{Mo}^{6+}$  peak could also be related to the oxidation of the  $\text{MoS}_2$  surface after the annealing from the exposure to the air environment.<sup>22</sup> In the experiment in this study, the oxygen percentage that bonded to the  $\text{MoS}_2$  surface could not be measured due to the use of  $\text{SiO}_2$  as the substrate. If the Mo in  $\text{MoS}_2$  is bonded with oxygen, the binding energy of the oxygen-adsorbed Mo in  $\text{MoS}_2$  (after the top S atoms are removed) decreases from 2.616 to 1.986 eV (Figure S10 and Table S5); however, this is still much higher than that (1.630 eV) of the Cl-adsorbed Mo in  $\text{MoS}_2$  (after the top S atoms are removed). Therefore, removing the Mo atoms from  $\text{MoS}_2$  after the subsequent  $\text{Ar}^+$ -ion exposure of 200 s is still difficult. In Mo ALE, Cl-radical adsorption onto Mo is consequently important for the preferential removal of Mo from the  $\text{MoS}_2$  structure.

Figure 3a shows the XPS data of Mo and S for the pristine bilayer  $\text{MoS}_2$  and the Cl-adsorbed bilayer  $\text{MoS}_2$ . After Cl-radical adsorption, the XPS peak intensities of Mo 3d and S 2p were decreased because of the presence of 58.5% of Cl on the  $\text{MoS}_2$  surface. In addition, the XPS peak positions of Mo  $3\text{d}_{3/2}$ , Mo  $3\text{d}_{5/2}$ , S  $2\text{p}_{1/2}$ , and S  $2\text{p}_{3/2}$  that are located at 232.4, 229.2, 163, and 162 eV, respectively, were blue-shifted by approximately +0.3 to +0.4 eV because of the Fermi-level increase caused by the movement of electrons from Mo and S to Cl with a higher electronegativity.<sup>23,24</sup> Figure 3b shows the XPS narrow-scan data for Cl in the pristine bilayer  $\text{MoS}_2$  and the Cl-adsorbed bilayer  $\text{MoS}_2$  after the  $\text{Ar}^+$ -ion exposure from 0 to 200 s. As shown, the Cl-peak intensity on the Cl-adsorbed bilayer  $\text{MoS}_2$  rapidly decreased from 0 to 30 s, followed by a gradual decrease from 30 to 60 s and a slow decrease to zero from 60 to 120 s. After the  $\text{Ar}^+$ -ion exposure time from 120 to 200 s, the Cl-related peak was not observed.

Figure 3c–f shows the XPS data of Mo and S for the  $\text{MoS}_2$  surface during the  $\text{Ar}^+$ -ion desorption step of  $\text{MoS}_2$  ALE after Cl adsorption. As shown in Figure 3c,e, after the  $\text{Ar}^+$ -ion exposure of the Cl-adsorbed bilayer  $\text{MoS}_2$ , the XPS peak positions were red-shifted back to the original pristine XPS positions due to the removal of the Cl atoms on the bilayer  $\text{MoS}_2$  surface (Figure S11). Figure 3c shows the XPS narrow-scan data of Mo and S after the  $\text{Ar}^+$ -ion exposure from 0 to 30 s; these data are related to the removal period of the top S atoms of the first  $\text{MoS}_2$  layer. During the  $\text{Ar}^+$ -ion exposure from 0 to 30 s, the peak intensities of Mo  $3\text{d}_{3/2}$  and Mo  $3\text{d}_{5/2}$  did not

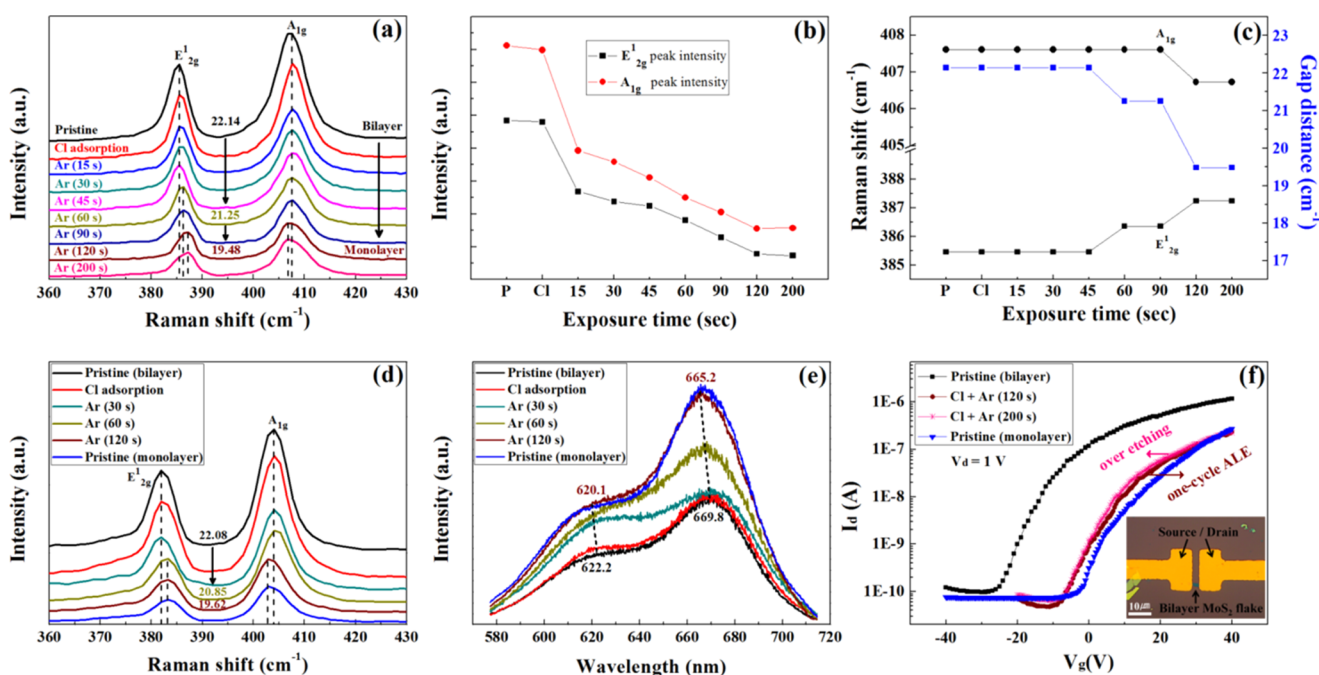
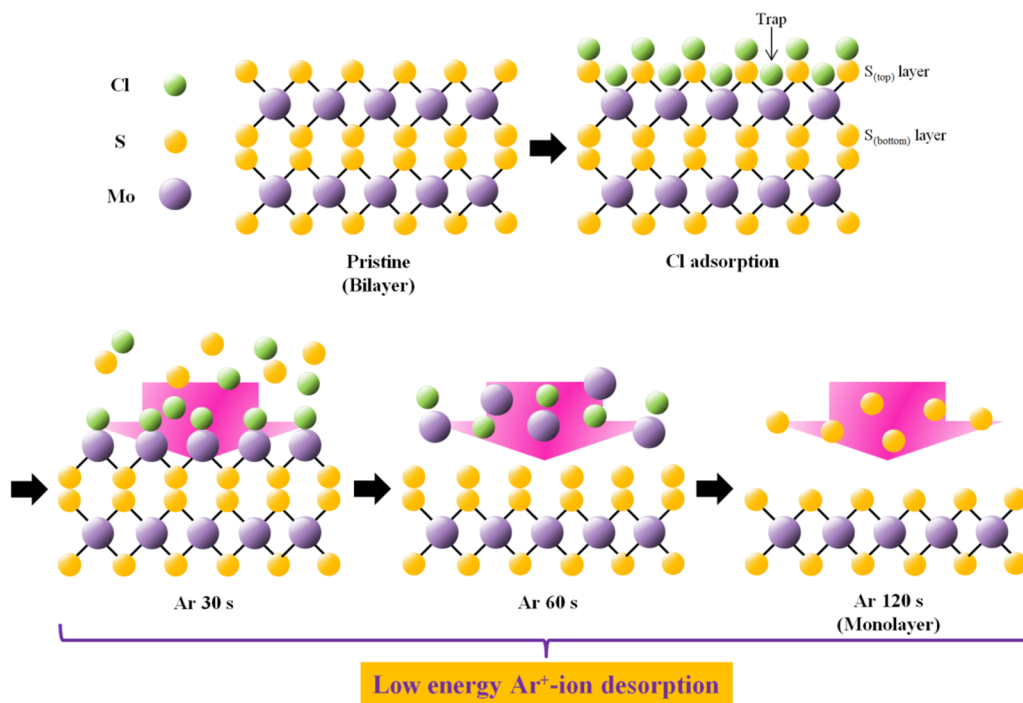
change, whereas the peak intensities of the S  $2\text{p}_{1/2}$  and S  $2\text{p}_{3/2}$  decreased due to the removal of the top S atoms on the first  $\text{MoS}_2$  layer, in addition to the red-shifting of the peak positions of Mo and S by approximately  $-0.2$  to  $-0.3$  eV, which is due to the removal of some of the Cl atoms with the top S atoms.

Figure 3d shows the XPS narrow-scan data of Mo and S after  $\text{Ar}^+$ -ion exposure from 30 to 60 s; these data are related to the Mo atom removal period of the first  $\text{MoS}_2$  layer. As the  $\text{Ar}^+$ -ion exposure time was increased from 30 to 60 s, the peak intensities of Mo  $3\text{d}_{3/2}$  and Mo  $3\text{d}_{5/2}$  decreased due to the removal of the Mo atoms in the first  $\text{MoS}_2$  layer, whereas the peak intensities of S  $2\text{p}_{1/2}$  and S  $2\text{p}_{3/2}$  were increased due to the exposure of the bottom S atoms of the first  $\text{MoS}_2$  layer. The peak positions of Mo and S were further red-shifted by approximately  $-0.1$  eV due to the removal of Cl. Also, the peak intensity of S—Mo—S at  $\sim 226.8$  eV, which is related to the crystalline  $\text{MoS}_2$ , was significantly decreased without an increase of the peak intensity of  $\text{Mo}^{6+}$  at  $\sim 236$  eV, which is related to the defective  $\text{MoS}_2$ . In general, when the  $\text{MoS}_2$  layer is physically damaged, the S—Mo—S peak intensity at  $\sim 226.8$  eV, which is related to the crystalline  $\text{MoS}_2$ , was decreased, and the  $\text{Mo}^{6+}$  peak intensity at  $\sim 236$  eV that is related to the damaged  $\text{MoS}_2$  is increased.<sup>21,22,25–27</sup> It is believed that the lack of increase of the  $\text{Mo}^{6+}$  peak intensity while the S—Mo—S peak intensity decreased during  $\text{MoS}_2$  ALE is related to the removal of Mo by Mo—Cl, whereby the first  $\text{MoS}_2$  layer is undamaged even though only the (Cl)—Mo bottom-S-atom bonding remains in the first  $\text{MoS}_2$  layer.

Figure 3e shows the XPS narrow-scan data of Mo and S after the  $\text{Ar}^+$ -ion exposure from 60 to 120 s that is related to the removal period of the bottom S atoms of the first  $\text{MoS}_2$  layer. During the  $\text{Ar}^+$ -ion exposure from 60 to 120 s, the peak intensities of Mo and S were gradually increased (in fact, the relative S intensity is decreased when it is normalized with the Mo peaks, which is due to the removal of the remaining bottom S atoms of the first  $\text{MoS}_2$  layer) without changing the peak positions of Mo and S. This indicates the gradual exposure of the second  $\text{MoS}_2$  layer as the top layer (as monolayer  $\text{MoS}_2$  from bilayer  $\text{MoS}_2$ ) through the removal of the remaining bottom S atoms of the first  $\text{MoS}_2$  layer that bonded with the second  $\text{MoS}_2$  layer through the van der Waals force. In addition, along with the evidence of the exposure of the second  $\text{MoS}_2$  layer, with the increase of the  $\text{Ar}^+$ -ion exposure time from 60 to 120 s, the crystalline S—Mo—S peak at  $\sim 226.8$  eV was increased without showing the defective  $\text{Mo}^{6+}$  peak at  $\sim 236$  eV. Also, the XPS peak-intensity ratios of Mo and S for the Cl-adsorbed bilayer  $\text{MoS}_2$  after the  $\text{Ar}^+$ -ion exposure of 120 s are similar to those of the pristine  $\text{MoS}_2$  layer (the peak ratios are the same for both the  $\text{MoS}_2$  bilayer and the  $\text{MoS}_2$  monolayer). Changes of the peak positions of Mo and S are not noticeable during the  $\text{Ar}^+$ -ion exposure from 60 to 120 s, and this is related to the fact that a significant amount of adsorbed Cl did not remain on the  $\text{MoS}_2$  layer, with the possible exception of some of the bottom S atoms of the first  $\text{MoS}_2$  layer. In fact, after the  $\text{Ar}^+$ -ion exposure time of 60 s, the XPS positions of Mo and S had shifted back to the locations that are similar to the positions of pristine  $\text{MoS}_2$  due to the removal of most of the Cl atoms that were adsorbed onto the  $\text{MoS}_2$  surface.

The remaining  $\text{MoS}_2$  layer became a monolayer  $\text{MoS}_2$ , and the  $\text{MoS}_2$  layer was further exposed to the  $\text{Ar}^+$  ions from 120 to 200 s. As shown in Figure 3f, even after the  $\text{Ar}^+$ -ion exposure of 200 s, changes of the peak intensities and peak positions of Mo and S were not observed, indicating that the  $\text{MoS}_2$  structure

**Scheme 1.** Schematic Diagram of the MoS<sub>2</sub> ALE Mechanism through Cl-Radical Adsorption and Ar<sup>+</sup>-Ion Desorption as a Function of Time



**Figure 4.** (a) Raman spectra of the CVD bilayer MoS<sub>2</sub> before and after Cl adsorption and those after the Ar<sup>+</sup>-ion exposure from 15 to 200 s. (b) Raman peak intensities of E<sup>1</sup><sub>2g</sub> and A<sub>1g</sub> of MoS<sub>2</sub>. (c) Peak positions of E<sup>1</sup><sub>2g</sub> and A<sub>1g</sub> of MoS<sub>2</sub> and the gap distance between E<sup>1</sup><sub>2g</sub> and A<sub>1g</sub>. (d) Raman and (e) photoluminescence (PL) spectra of the exfoliated bilayer MoS<sub>2</sub> and the exfoliated monolayer MoS<sub>2</sub> flakes. The Raman and PL spectra of the exfoliated bilayer MoS<sub>2</sub> flake before and after Cl adsorption and those after the Ar<sup>+</sup>-ion exposure from 30 to 120 s, exhibiting the formation of the monolayer MoS<sub>2</sub> from the bilayer MoS<sub>2</sub>, are also shown. (f) Drain currents vs gate voltages of the bottom-gate MoS<sub>2</sub> field effect transistors (FETs) that were fabricated with the exfoliated bilayer MoS<sub>2</sub>, the exfoliated monolayer MoS<sub>2</sub>, and the exfoliated bilayer MoS<sub>2</sub> after one cycle of MoS<sub>2</sub> ALE with 120 s (monolayer etching condition) and 200 s (overexposure with Ar<sup>+</sup>-ion) of Ar<sup>+</sup>-ion exposure. The inset shows an optical microscopic image of the bottom-gate MoS<sub>2</sub> FET that was fabricated with the exfoliated bilayer MoS<sub>2</sub>.

also remained unchanged. Also, because of the absence of any MoS<sub>2</sub> surface damage from the low-energy Ar<sup>+</sup>-ion exposure (approximately 20 eV), a change of the crystalline-S—Mo—S peak intensity and the existence of a defective Mo<sup>6+</sup> peak were

not observed, even though the MoS<sub>2</sub> layer was exposed by the 200 s of Ar<sup>+</sup> ions. Therefore, clean and undamaged monolayer MoS<sub>2</sub> was exposed after the one-cycle of ALE of the bilayer MoS<sub>2</sub>.

**Scheme 1** shows a schematic diagram of the detailed MoS<sub>2</sub> ALE mechanism for the one-cycle ALE from the bilayer MoS<sub>2</sub> to the monolayer MoS<sub>2</sub> through Cl-radical adsorption and Ar<sup>+</sup>-ion desorption. When Cl atoms were adsorbed on the bilayer MoS<sub>2</sub>, these were adsorbed on the top S atoms of MoS<sub>2</sub>, where they are also trapped between the top S atoms and the Mo atoms by the van der Waals force because six of the electrons in the Mo atoms (4d<sup>5</sup>Ss<sup>1</sup>) are fully bound to the S atoms. After Cl-radical adsorption, the binding energy between S<sub>(top)</sub> and Mo (the binding between the S 3s<sup>2</sup>3p<sup>4</sup> and Mo 4d<sup>5</sup>Ss<sup>1</sup>) decreased significantly (the binding energy of the top S atoms decreased from 1.99 to 1.47 eV) due to the higher electronegativity of Cl compared to that of S. Therefore, during the Ar<sup>+</sup>-ion desorption, the top S atoms of the first MoS<sub>2</sub> layer are preferentially removed as S—Cl for the Ar<sup>+</sup>-ion desorption time from 0 to 30 s. After the removal of the top S atoms, the trapped Cl atoms form Mo—Cl bonding, the binding energy between the Mo atoms and the bottom S atoms is significantly decreased (the binding energy of the Mo atoms decreased from 2.15 to 1.63 eV), and Mo is preferentially removed as Mo—Cl for the Ar<sup>+</sup>-ion desorption time from 30 to 60 s. After the removal of the top S and Mo atoms of the first MoS<sub>2</sub> layer, only the bottom S atoms that bonded with the second MoS<sub>2</sub> layer through the van der Waals force remain, and their binding energy decreased after the removal of the Mo atoms (the binding energy of the bottom S atoms decreased from 1.91 to 1.51 eV). Therefore, the bottom S atoms are finally removed during the Ar<sup>+</sup>-ion desorption time from 60 to 120 s. After the Ar<sup>+</sup>-ion exposure time of 120 s, the fresh second MoS<sub>2</sub> layer (bilayer to monolayer) is exposed, and because of the low Ar<sup>+</sup>-ion desorption energy of 20 eV, the further exposure to the Ar<sup>+</sup> ions does not change the exposed MoS<sub>2</sub> monolayer structure after the one-cycle MoS<sub>2</sub> ALE.

Figure 4a shows the Raman spectra of the CVD bilayer MoS<sub>2</sub> before and after Cl adsorption and after the Ar<sup>+</sup>-ion exposure from 15 to 200 s. The MoS<sub>2</sub> Raman spectra showed two peaks of E<sub>2g</sub><sup>1</sup> and A<sub>1g</sub>. It has previously been reported that not only their peak intensities decrease but also the gap differences between E<sub>2g</sub><sup>1</sup> and A<sub>1g</sub> decrease from ~22 to ~19 cm<sup>-1</sup> as the layer thickness was varied from the bilayer to monolayer.<sup>8,16–21,25</sup> As shown in Figure 4b, changes of the peak intensities of E<sub>2g</sub><sup>1</sup> and A<sub>1g</sub> were not observed after Cl-radical adsorption; however, after the Ar<sup>+</sup>-ion exposure, a decrease of the Raman peak intensities was observed up to 120 s of the Ar<sup>+</sup>-ion exposure and no further change of the peak intensities was observed after 120 s of the Ar<sup>+</sup>-ion exposure, indicating the decrease of the MoS<sub>2</sub> layer from the bilayer to the monolayer after 120 s of the Ar<sup>+</sup>-ion exposure. Measurement of the gap distances between E<sub>2g</sub><sup>1</sup> and A<sub>1g</sub> showed a decrease in the gaps after the Ar<sup>+</sup>-ion exposure, and the detailed changes of the peak positions of E<sub>2g</sub><sup>1</sup> and A<sub>1g</sub> are shown in Figure 4c. As shown, as the Ar<sup>+</sup>-ion exposure time was increased from 15 to 120 s, the gap distance decreased from ~22.14 to ~19.48 cm<sup>-1</sup>, indicating the change from a bilayer MoS<sub>2</sub> to monolayer MoS<sub>2</sub>. During the change from the bilayer MoS<sub>2</sub> to the monolayer MoS<sub>2</sub> from 60 to 90 s, the gap distance showed a midvalue of ~21.25 cm<sup>-1</sup>, which is possibly due to the changes of the interactions between the atoms from the S<sub>(top)</sub>—Mo—S<sub>(bottom)</sub> bonds to the Mo—S<sub>(bottom)</sub> bonds in the first MoS<sub>2</sub> layer during MoS<sub>2</sub> ALE.<sup>28</sup>

To investigate the degree of damage on the monolayer MoS<sub>2</sub> that occurred after the etching of the bilayer MoS<sub>2</sub> by the one-cycle MoS<sub>2</sub> ALE, bottom-gate MoS<sub>2</sub> FETs were fabricated with

the exfoliated pristine bilayer MoS<sub>2</sub>, the exfoliated pristine monolayer MoS<sub>2</sub>, and the exfoliated monolayer MoS<sub>2</sub> that were obtained using the one-cycle ALE of the exfoliated bilayer MoS<sub>2</sub>. In MoS<sub>2</sub>-FET fabrication, the exfoliated MoS<sub>2</sub> was used instead of the CVD MoS<sub>2</sub> because the exfoliated MoS<sub>2</sub> layers comprise a stoichiometric and defectless MoS<sub>2</sub>. With the exfoliated MoS<sub>2</sub> flakes, the bilayer and monolayer MoS<sub>2</sub> were selected by Raman spectroscopy, as shown in Figure 4d. One of the bilayer MoS<sub>2</sub> flakes was etched using the one-cycle MoS<sub>2</sub> ALE with different Ar<sup>+</sup>-ion exposure times from 30 (partial layer etch condition) to 120 s (monolayer etch condition), followed by the measurement of its Raman peak. The result is shown in Figure 4d. As shown in Figure 4d, the exfoliated pristine bilayer MoS<sub>2</sub> and the exfoliated pristine monolayer MoS<sub>2</sub> show typical gap distances between E<sub>2g</sub><sup>1</sup> and A<sub>1g</sub> of ~22.08 and ~19.62 cm<sup>-1</sup>, respectively. The monolayer MoS<sub>2</sub> that was obtained by the one-cycle ALE of the bilayer MoS<sub>2</sub> flake is ~19.62 cm<sup>-1</sup>, indicating the formation of the monolayer MoS<sub>2</sub>. In addition, the intensities and gap distances of the E<sub>2g</sub><sup>1</sup> and A<sub>1g</sub> peaks in the Raman spectra gradually decreased with Ar<sup>+</sup>-ion exposure from 30 to 120 s. These results are very similar to those of the CVD MoS<sub>2</sub> shown in Figure 4a.

Figure 4e shows the PL spectra of the exfoliated bilayer MoS<sub>2</sub>, exfoliated monolayer MoS<sub>2</sub>, exfoliated bilayer MoS<sub>2</sub> before and after Cl adsorption, and those after the Ar<sup>+</sup>-ion exposure from 30 to 120 s. Two peaks were observed in the PL spectra. The peak at ~665 nm was due to the direct band structure at the K point of the Brillouin zone, and the peak at ~620 nm was due to the splitting of the valence band from spin-orbit coupling.<sup>29,30</sup> The PL spectra were normalized by the Raman A<sub>1g</sub> peak intensity to avoid distortions caused by external environmental factors.<sup>13,31</sup> The PL intensity was almost unchanged after Cl adsorption on the bilayer MoS<sub>2</sub>, but the PL intensity gradually increased with Ar<sup>+</sup>-ion exposure from 30 to 120 s. Also, the PL peak position was gradually blue-shifted from 669.8 to 665.2 nm. These results are due to the band gap transitions from the indirect to the direct band gap according to the sequential removal of S<sub>(top)</sub>, Mo<sub>(mid)</sub>, and S<sub>(bottom)</sub>. In addition, the PL spectra of the exfoliated monolayer MoS<sub>2</sub> and the exfoliated bilayer MoS<sub>2</sub> after the one-cycle ALE are very similar, indicating that the single monolayer has been very effectively removed.

Using the exfoliated bilayer MoS<sub>2</sub>, exfoliated monolayer MoS<sub>2</sub>, and exfoliated bilayer MoS<sub>2</sub> after the one-cycle ALE with Ar<sup>+</sup>-ion exposure for 120 s (monolayer etch condition) to 200 s (overexposure condition), bottom-gate MoS<sub>2</sub> FETs were fabricated, and the characteristics of the drain currents versus the gate voltages ( $I_d$  vs  $V_g$ ) of the MoS<sub>2</sub> FETs are shown in Figure 4f. The inset shows an optical microscopic image of one of the ~3 μm channel bottom-gate MoS<sub>2</sub> FETs that were fabricated, for which 300 nm thick SiO<sub>2</sub> was used as the gate dielectric and 80 nm thick Au was used for the source and drain electrodes. As shown in Figure 4f, the MoS<sub>2</sub> FETs that were fabricated with the pristine bilayer MoS<sub>2</sub> and pristine monolayer MoS<sub>2</sub> exhibited the typical electrical characteristics of the MoS<sub>2</sub> FETs. Also, the MoS<sub>2</sub> FETs that were fabricated with MoS<sub>2</sub> and obtained after the one-cycle ALE of the bilayer MoS<sub>2</sub> with Ar<sup>+</sup>-ion exposure of 120 and 200 s exhibited similar electrical characteristics as those of the FETs fabricated with a pristine monolayer MoS<sub>2</sub>. The field-effect mobility ( $\mu$ ) of the fabricated MoS<sub>2</sub> FETs was calculated using the following equation:  $\mu = (dI_d/dV_g) \times [L/(WC_iV_d)]$ , where  $L$  is the channel length and  $W$  is the channel width ( $L$  and  $W$  were

obtained from the SEM images of the fabricated MoS<sub>2</sub> FETs).  $C_i = 1.151 \times 10^{-4}$  F m<sup>-2</sup> is the back-gate capacitance ( $C = \epsilon_0 \epsilon_r / d$ ;  $\epsilon_0 = 8.85 \times 10^{-12}$  F m<sup>-1</sup>,  $\epsilon_r = 3.9$ , and  $d = 300$  nm), which was calculated by assuming a parallel plate capacitance model.<sup>32,33</sup> The calculated field effect mobility of the exfoliated bilayer MoS<sub>2</sub> (black), the exfoliated monolayer MoS<sub>2</sub> (blue), and the exfoliated bilayer MoS<sub>2</sub> after the one-cycle MoS<sub>2</sub> ALE under the monolayer etching condition (120 s, brown) and Ar<sup>+</sup> ion overexposure condition (200 s, pink) were estimated to be 5.78, 2.65, 2.03, and 2.02 cm<sup>2</sup> V<sup>-1</sup> s<sup>-1</sup>, respectively. The mobility differences between the exfoliated pristine monolayer MoS<sub>2</sub> and the monolayer MoS<sub>2</sub> after ALE with 120 and 200 s of Ar<sup>+</sup>-ion exposure were similar and were in the error range. Therefore, one-monolayer MoS<sub>2</sub> could be successfully removed by the MoS<sub>2</sub> ALE process without damaging the MoS<sub>2</sub> layer.

## CONCLUSIONS

The single MoS<sub>2</sub> monolayer has a S<sub>(top)</sub>—Mo—S<sub>(bottom)</sub> crystal structure that consists of three-atom-thick covalent bonds between the Mo and S atoms; therefore, the ALE mechanism for which Cl is used as the adsorption species and the Ar<sup>+</sup> ion is used as the desorption species can differ somewhat from that of other two-dimensional (2D) materials with one-atom-thick bonds, such as graphene. The MoS<sub>2</sub> ALE mechanism from the bilayer MoS<sub>2</sub> to the monolayer MoS<sub>2</sub>, for which controlled Cl-radical adsorption and Ar<sup>+</sup>-ion desorption are used, was investigated in this article as a function of the Ar<sup>+</sup>-ion desorption time with a monoenergetic Ar<sup>+</sup>-ion energy of 20 eV. The results showed that the Cl atoms are adsorbed on the top S atoms and are trapped between the top S atoms and the Mo atoms by the van der Waals force during Cl-radical adsorption. The results also showed that the monolayer MoS<sub>2</sub> is sequentially removed from the top S atoms by S—Cl, Mo is removed by Mo—Cl, and the bottom S atoms are removed by selective sputtering. The XPS data showed no change of chemical composition and no structural damage to the exposed second MoS<sub>2</sub> layer after the one-cycle ALE. In addition, the MoS<sub>2</sub> FETs fabricated with the MoS<sub>2</sub> samples obtained after the one-cycle ALE (monolayer etch condition and Ar<sup>+</sup>-ion overexposure condition) of a bilayer MoS<sub>2</sub> exhibited similar electrical properties to those fabricated with a pristine monolayer MoS<sub>2</sub>. Therefore, ALE technology can effectively and precisely remove MoS<sub>2</sub> layers layer-by-layer without electrical damage to the remaining MoS<sub>2</sub> layers. It is believed that the ALE technique used in the experiment can be applicable to all of the layered TMD materials including MoS<sub>2</sub> for next-generation nanodevices.

## MATERIALS AND METHODS

**Formation of the Bilayer MoS<sub>2</sub>.** For the MoS<sub>2</sub> ALE mechanism study, bilayer MoS<sub>2</sub> films were synthesized by CVD. For the fabrication of MoS<sub>2</sub> device, bilayer- and monolayer-MoS<sub>2</sub> flakes (for stoichiometric and zero-defect MoS<sub>2</sub>) were obtained by mechanical exfoliation from bulk MoS<sub>2</sub>. To improve the hydrophilic property of the substrate surface, a 300 nm thick SiO<sub>2</sub>/heavily p-type-doped Si wafer was treated in capacitively coupled plasma equipment with an oxygen plasma under the condition of 5 sccm of O<sub>2</sub> and 60 W for 120 s before MoS<sub>2</sub> formation. For the CVD of MoS<sub>2</sub>, the bilayer MoS<sub>2</sub> films were synthesized in a vacuum furnace through vaporizing MoO<sub>3</sub> and sulfur for 20 min, while the substrate was heated to 800 °C. For the exfoliated MoS<sub>2</sub>, the MoS<sub>2</sub> flakes were mechanically exfoliated from the bulk MoS<sub>2</sub> using Scotch tape, and they were then placed onto the 300 nm thick SiO<sub>2</sub>/heavily p-type-doped Si wafer. The bilayer- and monolayer-MoS<sub>2</sub> flakes were obtained using optical microscopy, and

the thickness of the candidates was confirmed by Raman spectroscopy (HORIBA, ARAMS).

**MoS<sub>2</sub> ALE Method.** First, the Cl radicals that were generated from the ICP system were adsorbed onto the MoS<sub>2</sub> surface. Then, the chlorinated MoS<sub>2</sub> surface was removed using a low-energy Ar<sup>+</sup>-ion beam system. During Cl-radical adsorption, the ion bombardment to the MoS<sub>2</sub> surface was significantly reduced by a grounded metal-mesh grid installed between the ICP source and the substrate. For Cl-radical adsorption, Cl<sub>2</sub> plasma was generated for 120 s at 10 mTorr with 63 sccm of Cl<sub>2</sub> and 18 W of a 13.56 MHz radio frequency (rf) ICP-source power. For the MoS<sub>2</sub> desorption step, the Cl-radical-adsorbed MoS<sub>2</sub> samples were transferred to a dual grid, ICP-type Ar<sup>+</sup>-ion-beam system. The Cl-radical-adsorbed MoS<sub>2</sub> monolayer was then removed for 120 s with an Ar<sup>+</sup>-ion beam, while the inside extraction-grid voltage was maintained at +10 V (~20 eV of Ar<sup>+</sup>-ion peak energy; see Figure S1a) for the acceleration of the Ar<sup>+</sup> ion, whereas the outside grid of the ion-beam system was grounded. The process conditions are Ar of 70 sccm, a 13.56 MHz ICP power of 200 W, and pressure of 6.7 mTorr. The details of the mesh-gridded ICP system for Cl-radical adsorption and the Ar<sup>+</sup>-ion-beam system for MoS<sub>2</sub> desorption can be found elsewhere.<sup>21</sup>

**MoS<sub>2</sub> Binding-Energy Calculation.** To theoretically investigate the mechanism of MoS<sub>2</sub> ALE according to the adsorption of Cl radicals on MoS<sub>2</sub> and desorption by Ar<sup>+</sup>-ion bombardment, a computer simulation was performed for the changing of the binding energies between Mo and S using the Vienna Ab Initio Simulation Package.<sup>34</sup> The lattice constant of the MoS<sub>2</sub> unit cell was calculated as 3.213 Å, the distance between top S and bottom S as 3.159 Å, and the bond length of Mo—S as 2.436 Å. To describe the MoS<sub>2</sub> multilayer system, a 2D periodic boundary condition was used along the growth direction with a vacuum layer of 27 Å along the nonperiodic direction to avoid an additional interaction between the multilayers. Spin-unpolarized density function theory calculations were performed with the Perdew–Burke–Ernzerhof generalized gradient approximation (PBE-GGA)<sup>35</sup> and the projector-augmented wave (PAW)<sup>36</sup> method. Geometry optimization was performed on the 3 × 3 × 1 supercell structure, with a 3 × 3 × 1 Monkhorst–Pack *k*-point<sup>37</sup> mesh and plane-wave basis sets with an energy cutoff of 400 eV. The convergence threshold for the energy was set to 10<sup>-4</sup> eV. The Mo—S binding energy ( $E_B$ ) was calculated using  $E_B = (E_{\text{tot}} - E_{\text{sub}} - E_S - E_{\text{vdw}})/n$ , where  $E_{\text{tot}}$ ,  $E_{\text{sub}}$ ,  $E_S$ ,  $E_{\text{vdw}}$ , and  $n$  refer to the electronic energy of the entire system, the energy of the system after the removal of the target atom, the energy of the target atom, the van der Waals interaction energy, and the number of target atom coordination bonds, respectively. The van der Waals interaction energy between the target atom and the adjacent layer was calculated using  $E_{\text{vdw}} = (E_{\text{S+AL}} - E_{\text{AL}} - E_S)$ , where  $E_{\text{S+AL}}$  and  $E_{\text{AL}}$  represent the electronic energy of the adjacent layer with the target atom held together and the energy of the adjacent layer, respectively (Figure S2). For the MoS<sub>2</sub> bilayer structure, both the A–A and A–B stacking structures were considered (Figures S3 and S8).

**MoS<sub>2</sub>-FET Fabrication.** For the MoS<sub>2</sub>-FET fabrication, few-layer MoS<sub>2</sub> was exfoliated and transferred to a SiO<sub>2</sub>/Si wafer. Bilayer- and monolayer-MoS<sub>2</sub> flakes were obtained using optical microscopy, and the thickness of the MoS<sub>2</sub> layer was confirmed by Raman spectroscopy (HORIBA, ARAMS). For the bottom-gate FET fabrication, the conventional photolithography method was used to define the source/drain electrode contact area with a ~3 μm channel region and 80 nm thick Au was deposited by a thermal evaporation system. After a lift-off process, contact annealing (Ar: 96.1%, H<sub>2</sub>: 3.9%, 1 slm, and 200 °C for 1 h) was performed prior to measurement to increase the contact property of the devices.

**Characterization.** The Raman and PL spectra were inspected using a Raman microscopic system (WITEC α 300 M<sup>+</sup>) with a wavelength of 532 nm. The morphology of the MoS<sub>2</sub> surface was measured by atomic force microscopy (AFM, Dimension 3100, Veeco) under the tapping mode. The chemical composition of the MoS<sub>2</sub> surface was measured by XPS (MultiLab 2000, Thermo VG, Mg Kα source). During the XPS measurement, to observe the S/Mo ratio, the take-off angle of the MoS<sub>2</sub> sample was maintained at 45° and the

peak energies were calibrated using the C1 peak at 284.5 eV. The electrical characteristics of the MoS<sub>2</sub> FET were measured under ambient conditions using Keithley 4200-SCS. The change of the thickness of the MoS<sub>2</sub> layer before and after the ALE cycles was observed using field-emission transmission electron microscopy (JEOL JEM-2100F).

## ASSOCIATED CONTENT

### Supporting Information

The Supporting Information is available free of charge on the ACS Publications website at DOI: [10.1021/acsami.6b15886](https://doi.org/10.1021/acsami.6b15886).

Calculation of binding energy according to Cl-radical adsorption and Ar<sup>+</sup>-ion desorption on the bilayer MoS<sub>2</sub> structure (A-A stacking and A-B stacking) and additional experimental data ([PDF](#))

## AUTHOR INFORMATION

### Corresponding Authors

\*E-mail: [ggyeom@skku.edu](mailto:ggyeom@skku.edu) (G.Y.Y.).

\*E-mail: [plasma@skku.edu](mailto:plasma@skku.edu) (D.W.K.).

### ORCID

Jin Yong Lee: [0000-0003-0360-5059](https://orcid.org/0000-0003-0360-5059)

Sung Joo Lee: [0000-0003-1284-3593](https://orcid.org/0000-0003-1284-3593)

Yeon Sik Jung: [0000-0002-7709-8347](https://orcid.org/0000-0002-7709-8347)

Geun Young Yeom: [0000-0001-7516-8404](https://orcid.org/0000-0001-7516-8404)

### Notes

The authors declare no competing financial interest.

## ACKNOWLEDGMENTS

This work was supported by the Nano-Material Technology Development Program through the National Research Foundation of Korea (NRF), funded by the Ministry of Education, Science and Technology (2012M3A7B4035323 and 2016M3A7B4910429).

## REFERENCES

- (1) Baugher, B. W.; Churchill, H. O.; Yang, Y.; Jarillo-Herrero, P. Optoelectronic Devices Based on Electrically Tunable pn Diodes in a Monolayer Dichalcogenide. *Nat. Nanotechnol.* **2014**, *9*, 262–267.
- (2) Jariwala, D.; Sangwan, V. K.; Lauhon, L. J.; Marks, T. J.; Hersam, M. C. Emerging Device Applications for Semiconducting Two-dimensional Transition Metal Dichalcogenides. *ACS Nano* **2014**, *8*, 1102–1120.
- (3) Wang, Q. H.; Kalantar-Zadeh, K.; Kis, A.; Coleman, J. N.; Strano, M. S. Electronics and Optoelectronics of Two-dimensional Transition Metal Dichalcogenides. *Nat. Nanotechnol.* **2012**, *7*, 699–712.
- (4) Geim, A. K.; Grigorieva, I. V. Van der Waals Heterostructures. *Nature* **2013**, *499*, 419–425.
- (5) Lee, C.; Yan, H.; Brus, L. E.; Heinz, T. F.; Hone, J.; Ryu, S. Anomalous Lattice Vibrations of Single-and Few-layer MoS<sub>2</sub>. *ACS Nano* **2010**, *4*, 2695–2700.
- (6) Li, B.; Yang, S.; Huo, N.; Li, Y.; Yang, J.; Li, R.; Fan, C.; Lu, F. Growth of Large Area Few-layer or Monolayer MoS<sub>2</sub> from Controllable MoO<sub>3</sub> Nanowire Nuclei. *RSC Adv.* **2014**, *4*, 26407–26412.
- (7) Yang, S.; Kang, J.; Yue, Q.; Yao, K. Vapor Phase Growth and Imaging Stacking Order of Bilayer Molybdenum Disulfide. *J. Phys. Chem. C* **2014**, *118*, 9203–9208.
- (8) Huang, Y.; Wu, J.; Xu, X.; Ho, Y.; Ni, G.; Zou, Q.; Koon, G. K. W.; Zhao, W.; Neto, A. C.; Eda, G.; et al. An Innovative Way of Etching MoS<sub>2</sub>: Characterization and Mechanistic Investigation. *Nano Res.* **2013**, *6*, 200–207.
- (9) Mak, K. F.; Lee, C.; Hone, J.; Shan, J.; Heinz, T. F. Atomically Thin MoS<sub>2</sub>: A New Direct-gap Semiconductor. *Phys. Rev. Lett.* **2010**, *105*, No. 136805.
- (10) Frey, G.; Elani, S.; Homyonfer, M.; Feldman, Y.; Tenne, R. Optical-absorption Spectra of Inorganic Fullerene-like MS<sub>2</sub> (M=Mo, W). *Phys. Rev. B* **1998**, *57*, No. 6666.
- (11) Kam, K.; Parkinson, B. Detailed Photocurrent Spectroscopy of the Semiconducting Group VIIB Transition Metal Dichalcogenides. *J. Phys. Chem.* **1982**, *86*, 463–467.
- (12) Liu, K.; Zhang, W.; Lee, Y.; Lin, Y.; Chang, M.; Su, C.; Chang, C.; Li, H.; Shi, Y.; Zhang, H.; et al. Growth of Large-area and Highly Crystalline MoS<sub>2</sub> Thin Layers on Insulating Substrates. *Nano Lett.* **2012**, *12*, 1538–1544.
- (13) Jeon, J.; Jang, S. K.; Jeon, S. M.; Yoo, G.; Jang, Y. H.; Park, J.; Lee, S. Layer-controlled CVD Growth of Large-area Two-dimensional MoS<sub>2</sub> Films. *Nanoscale* **2015**, *7*, 1688–1695.
- (14) Dumcenco, D.; Ovchinnikov, D.; Marinov, K.; Lazic, P.; Gibertini, M.; Marzari, N.; Sanchez, O. L.; Kung, Y.; Krasnozhon, D.; Chen, M.; et al. Large-area Epitaxial Monolayer MoS<sub>2</sub>. *ACS Nano* **2015**, *9*, 4611–4620.
- (15) Kim, H.; Ahn, C.; Arabale, G.; Lee, C.; Kim, T. Synthesis of MoS<sub>2</sub> Atomic Layer using PECVD. *ECS Trans.* **2013**, *58*, 47–50.
- (16) Castellanos-Gomez, A.; Barkelid, M.; Goossens, A.; Calado, V. E.; van der Zant; van der Zant, H. S. J.; Steele, G. A. Laser-thinning of MoS<sub>2</sub>: On Demand Generation of a Single-layer Semiconductor. *Nano Lett.* **2012**, *12*, 3187–3192.
- (17) Xiao, S.; Xiao, P.; Zhang, X.; Yan, D.; Gu, X.; Qin, F.; Ni, Z.; Han, Z. J.; Ostrivov, K. K. Atomic-Layer Soft Plasma Etching of MoS<sub>2</sub>. *Sci. Rep.* **2016**, *6*, No. 19945.
- (18) Liu, Y.; Nan, H.; Wu, X.; Pan, W.; Wang, W.; Bai, J.; Zhao, W.; Sun, L.; Wang, X.; Ni, Z. Layer-by-layer Thinning of MoS<sub>2</sub> by Plasma. *ACS Nano* **2013**, *7*, 4202–4209.
- (19) Lu, X.; Utama, M. I. B.; Zhang, J.; Zhao, Y.; Xiong, Q. Layer-by-layer Thinning of MoS<sub>2</sub> by Thermal Annealing. *Nanoscale* **2013**, *5*, 8904–8908.
- (20) Wu, J.; Li, H.; Yin, Z.; Li, H.; Liu, J.; Cao, X.; Zhang, Q.; Zhang, H. Layer Thinning and Etching of Mechanically Exfoliated MoS<sub>2</sub> Nanosheets by Thermal Annealing in Air. *Small* **2013**, *9*, 3314–3319.
- (21) Lin, T.; Kang, B.; Jeon, M.; Huffman, C.; Jeon, J.; Lee, S.; Han, W.; Lee, J.; Lee, S.; Yeom, G.; Kim, K. Controlled Layer-by-layer Etching of MoS<sub>2</sub>. *ACS Appl. Mater. Interfaces* **2015**, *7*, 15892–15897.
- (22) Yang, X.; Fu, W.; Liu, W.; Hong, J.; Cai, Y.; Jin, C.; Xu, M.; Wang, H.; Yang, D.; Chen, H. Engineering Crystalline Structures of Two-dimensional MoS<sub>2</sub> Sheets for High-performance Organic Solar Cells. *J. Mater. Chem. A* **2014**, *2*, 7727–7733.
- (23) Yang, L.; Majumdar, K.; Liu, H.; Du, Y.; Wu, H.; Hatzistergos, M.; Hung, P.; Tieckelmann, R.; Tsai, W.; Hobbs, C.; Ye, P. D. Chloride Molecular Doping Technique on 2D Materials: WS<sub>2</sub> and MoS<sub>2</sub>. *Nano Lett.* **2014**, *14*, 6275–6280.
- (24) Yang, L.; Majumdar, K.; Du, Y.; Liu, H.; Wu, H.; Hatzistergos, M.; Hung, P.; Tieckelmann, R.; Tsai, W.; Hobbs, C. In *High-performance MoS<sub>2</sub> Field-effect Transistors Enabled by Chloride Doping: Record Low Contact Resistance (0.5 kΩ· μm) and Record High Drain Current (460 μA/μm)*; Symposium on VLSI Technology (VLSI-Technology): Digest of Technical Papers; IEEE, 2014; pp 1–2.
- (25) Jeon, M. H.; Ahn, C.; Kim, H.; Kim, K. N.; Lin, T. Z.; Qin, H.; Kim, Y.; Lee, S.; Kim, T.; Yeom, G. Y. Controlled MoS<sub>2</sub> Layer Etching using CF<sub>4</sub> Plasma. *Nanotechnology* **2015**, *26*, No. 355706.
- (26) Baker, M.; Gilmore, R.; Lenardi, C.; Gissler, W. XPS Investigation of Preferential Sputtering of S from MoS<sub>2</sub> and Determination of MoS<sub>x</sub> Stoichiometry from Mo and S Peak Positions. *Appl. Surf. Sci.* **1999**, *150*, 255–262.
- (27) Ma, Q.; Odenthal, P. M.; Mann, J.; Le, D.; Wang, C. S.; Zhu, Y.; Chen, T.; Sun, D.; Yamaguchi, K.; Tran, T.; et al. Controlled Argon Beam-induced Desulfurization of Monolayer Molybdenum Disulfide. *J. Phys.: Condens. Matter* **2013**, *25*, No. 252201.
- (28) Wieting, T.; Verble, J. Interlayer Bonding and the Lattice Vibrations of β-GaSe. *Phys. Rev. B* **1972**, *5*, No. 1473.

- (29) Splendiani, A.; Sun, L.; Zhang, Y.; Li, T.; Kim, J.; Chim, C.; Galli, G.; Wang, F. Emerging Photoluminescence in Monolayer MoS<sub>2</sub>. *Nano Lett.* **2010**, *10*, 1271–1275.
- (30) Zhu, Z.; Cheng, Y.; Schwingenschlögl, U. Giant Spin-Orbit-Induced Spin Splitting in Two-Dimensional Transition-Metal Dichalcogenide Semiconductors. *Phys. Rev. B* **2011**, *84*, No. 153402.
- (31) Mak, K. F.; Lee, C.; Hone, J.; Shan, J.; Heinz, T. F. Atomically Thin MoS<sub>2</sub>: A New Direct-Gap Semiconductor. *Phys. Rev. Lett.* **2010**, *105*, No. 136805.
- (32) Lopez-Sanchez, O.; Lembke, D.; Kayci, M.; Radenovic, A.; Kis, A. Ultrasensitive Photodetectors Based on Monolayer MoS<sub>2</sub>. *Nat. Nanotechnol.* **2013**, *8*, 497–501.
- (33) Fang, H.; Tosun, M.; Seol, G.; Chang, T. C.; Takei, K.; Guo, J.; Javey, A. Degenerate N-Doping of Few-Layer Transition Metal Dichalcogenides by Potassium. *Nano Lett.* **2013**, *13*, 1991–1995.
- (34) Kresse, G.; Furthmüller, J. Efficiency of ab-initio Total Energy Calculations for Metals and Semiconductors using a Plane-wave Basis Set. *Comput. Mater. Sci.* **1996**, *6*, 15–50.
- (35) Perdew, J. P.; Burke, K.; Ernzerhof, M. Generalized Gradient Approximation Made Simple. *Phys. Rev. Lett.* **1996**, *77*, No. 3865.
- (36) Blöchl, P. E. Projector Augmented-wave Method. *Phys. Rev. B: Condens. Matter Mater. Phys.* **1994**, *50*, No. 17953.
- (37) Monkhorst, H. J.; Pack, J. D. Special Points for Brillouin-zone Integrations. *Phys. Rev. B: Condens. Matter Mater. Phys.* **1976**, *13*, No. 5188.